Chemical Science

ROYAL SOCIETY OF CHEMISTRY

EDGE ARTICLE

View Article Online
View Journal | View Issue

Cite this: *Chem. Sci.*, 2022, **13**, 1382

All publication charges for this article have been paid for by the Royal Society of Chemistry

Surface environment complication makes Ag_{29} nanoclusters more robust and leads to their unique packing in the supracrystal lattice†

Chao Xu,‡[ab] Qianqin Yuan,‡[ab] Xiao Wei,[ab] Hao Li,[ab] Honglei Shen,[ab] Xi Kang *[ab] and Manzhou Zhu *[ab]

Received 1st November 2021
Accepted 31st December 2021

DOI: 10.1039/d1sc06002c

rsc.li/chemical-science

Silver nanoclusters have received unprecedented attention in cluster science owing to their promising functionalities and intriguing physical/chemical properties. However, essential instability significantly impedes their extensive applications. We herein propose a strategy termed "surface environment complication" to endow Ag_{29} nanoclusters with high robustness. The $Ag_{29}(S\text{-}Adm)_{18}(PPh_3)_4$ nanocluster with monodentate PPh_3 ligands was extremely unstable and uncrystallizable. By substituting PPh_3 with bidentate PPh_2py with dual coordination sites (*i.e.*, P and N), the Ag_{29} cluster framework was twisted because of the generation of N–Ag interactions, and three NO_3 ligands were further anchored onto the nanocluster surface, yielding a new $Ag_{29}(S\text{-}Adm)_{15}(NO_3)_3(PPh_2py)_4$ nanocluster with high stability. The metal-control or ligand-control effects on stabilizing the Ag_{29} nanocluster were further evaluated. Besides, $Ag_{29}(S\text{-}Adm)_{15}(NO_3)_3(PPh_2py)_4$ followed a unique packing mode in the supracrystal lattice with several intercluster channels, which has yet been observed in other M_{29} cluster crystals. Overall, this work presents a new approach (*i.e.*, surface environment complication) for tailoring the surface environment and improving the stability of metal nanoclusters.

1 Introduction

Since the advent of metal nanoclusters with atomic precision, these novel nanomaterials have garnered significant interest because of their accurate compositions/constructions and intriguing physicochemical properties.[1–8] Indeed, owing to their quantum size effect and discrete electronic energy levels, metal nanoclusters and cluster-based nanomaterials display atomic structure tunable properties, that is, slight tailoring of structures of nanoclusters can trigger remarkable differences in their performances.[9–13] Besides, metal nanoclusters have been used as ideal platforms for the meticulous investigation of structure–property correlations.[14–20] Consequently, metal nanoclusters are an emerging class of programmable nanomaterials for several promising applications, such as catalysis, drug delivery, energy storage, and biological applications.[21–24]

In the past two decades, silver nanoclusters have received unprecedented attention in cluster science.[25–40] It is widely accepted that silver nanoclusters exhibit promising functionalities and intriguing physical/chemical properties that are obviously different from their gold counterparts.[27] Ag-based metal nanoclusters generally display strong photoluminescence that renders them optically active nanomaterials for sensors or biological applications.[41–43] However, Ag nanoclusters are essentially unstable relative to Au nanoclusters, which significantly impedes their extensive applications. Developing new approaches to enhance the nanocluster stability remains highly desired.

Recently, our group has developed a $M_{29}(S\text{-}Adm)_{18}(PPh_3)_4$ (where S-Adm is 1-adamantanethiol) nanocluster system for mapping the structure–property correlations at the atomic level.[44–46] Although several M_{29} nanoclusters, *e.g.*, $Pt_1Ag_{28}(S\text{-}Adm)_{18}(PPh_3)_4$ (**Pt_1Ag_{28}-PPh_3** for short), $Au_1Ag_{28}(S\text{-}Adm)_{18}(PPh_3)_4$, and $Pt_1Ag_{12}Cu_{16}(S\text{-}Adm)_{18}(PPh_3)_4$, have been controllably synthesized and structurally determined, the homometal $Ag_{29}(S\text{-}Adm)_{18}(PPh_3)_4$ (**Ag_{29}-PPh_3** for short) nanocluster was extremely unstable and uncrystallizable.[46] We remain committed to stabilizing the homo-silver Ag_{29} nanocluster with a new approach.

Herein, a "surface environment complication" strategy has been exploited to endow the Ag_{29} nanocluster with high robustness. By substituting the monodentate PPh_3 (with only the P coordination site) in previously reported **Ag_{29}-PPh_3** with

[a]*Department of Chemistry, Centre for Atomic Engineering of Advanced Materials, Anhui Province Key Laboratory of Chemistry for Inorganic/Organic Hybrid Functionalized Materials, Anhui University, Hefei 230601, P. R. China. E-mail: kangxi_chem@ahu.edu.cn*

[b]*Key Laboratory of Structure and Functional Regulation of Hybrid Materials, Anhui University, Ministry of Education, Hefei 230601, P. R. China. E-mail: zmz@ahu.edu.cn*

† Electronic supplementary information (ESI) available: Fig. S1–S12 for the crystal structure, ESI-MS and UV-vis results of nanoclusters. CCDC 2115749 and 2117814. For ESI and crystallographic data in CIF or other electronic format see DOI: 10.1039/d1sc06002c

‡ C. X. and Q. Y. contributed equally to this work.

bidentate PPh_2py (with P and N dual coordination sites), the nanocluster surface structure underwent a twist due to the generation of N–Ag interactions. Besides, three NO_3 ligands were further anchored onto the nanocluster surface, making the metallic kernel entirely wrapped. The obtained Ag_{29}(S-Adm)$_{15}(NO_3)_3(PPh_2py)_4$ (**Ag_{29}-PPh_2py** for short) nanocluster was much more robust relative to **Ag_{29}-PPh_3**, and its structure was successfully determined by single-crystal X-ray diffraction. Furthermore, based on this nanocluster template, the metal-control and ligand-control effects on stabilizing the Ag_{29} framework were evaluated. Moreover, at the supramolecular level, **Ag_{29}-PPh_2py** followed a unique packing mode in the crystal lattice with several intercluster channels, while such an aggregation pattern has yet been discovered in other M_{29} cluster crystals.

2 Experimental methods

Materials

All the following reagents were purchased from Sigma-Aldrich and used without further purification: silver nitrate ($AgNO_3$, 99.5%, metal basis), hexachloroplatinic(IV) acid ($H_2PtCl_6 \cdot 6H_2O$, 99.9% metals basis), 1-adamantanethiol (Adm-SH, $C_{10}H_{15}SH$, 99%), triphenylphosphine (PPh_3, 99%), diphenyl-2-pyridylphosphine (PPh_2py, 97%), sodium borohydride ($NaBH_4$, 99%), methylene chloride (CH_2Cl_2, HPLC grade), methanol (CH_3OH, HPLC grade), ethanol (CH_3CH_2OH, HPLC grade), and *n*-hexane (C_6H_{12}, HPLC grade).

Synthesis of Ag_{29}(S-Adm)$_{18}(PPh_3)_4$ (**Ag_{29}-PPh_3**)

The preparation of **Ag_{29}-PPh_3** was based on a reported method.[46]

Synthesis of Pt_1Ag_{28}(S-Adm)$_{18}(PPh_3)_4$ (**Pt_1Ag_{28}-PPh_3**)

The preparation of **Pt_1Ag_{28}-PPh_3** was based on a reported method.[46]

Preparation of Ag_{29}(S-Adm)$_{15}(NO_3)_3(PPh_2py)_4$ (**Ag_{29}-PPh_2py**)

In a 50 mL round-bottom flask, 94 mg of $AgNO_3$ was dissolved in 5 mL of MeOH and 10 mL of EtOH, and 50 mg of Adm-SH was added under vigorous stirring. After 20 min, 100 mg of PPh_2py was added. Shortly after this, 10 mg of $NaBH_4$ (dissolved in 1 mL of EtOH) was poured in, and the reaction was continued for 12 hours. The obtained solution was centrifuged at 10 000 rpm for 5 minutes, and then the supernatant was collected and evaporated to get the dry product, which was then washed several times with *n*-hexane to get the final product, *i.e.*, **Ag_{29}-PPh_2py**. The yield was about 30% based on the Ag element (calculated from $AgNO_3$).

Preparation of Pt_1Ag_{28}(S-Adm)$_{18}(PPh_2py)_4$ (**Pt_1Ag_{28}-PPh_2py**)

94 mg of $AgNO_3$ used to synthesize **Ag_{29}-PPh_2py** was substituted by 94 mg of $AgNO_3$ and 10 mg of $H_2PtCl_6 \cdot 6H_2O$. Other conditions remained unchanged. The yield for the synthesis of **Pt_1Ag_{28}-PPh_2py** was about 45% based on the Ag element (calculated from $AgNO_3$).

Crystallization of the Ag_{29} nanocluster series

Single crystals of **Ag_{29}-PPh_2py** or **Pt_1Ag_{28}-PPh_2py** were cultivated at −4 °C by liquid-diffusing *n*-hexane into the CH_2Cl_2 solution of each nanocluster. After a week, red crystals were collected, and the structures of these nanoclusters were determined. Of note, in order to accelerate the crystallization process and improve the crystal quality, the counterions (*i.e.*, Cl^-) in these nanoclusters were replaced by SbF_6^- or BPh_4^-.[47] The reaction equation was $[Ag_{29}(S\text{-}Adm)_{15}(NO_3)_3(PPh_2py)_4]Cl_3 + 3SbF_6^- \rightarrow [Ag_{29}(S\text{-}Adm)_{15}(NO_3)_3(PPh_2py)_4](SbF_6)_3 + 3Cl^-$ or $[Pt_1Ag_{28}(S\text{-}Adm)_{18}(PPh_2py)_4]Cl_2 + 2BPh_4^- \rightarrow [Pt_1Ag_{28}(S\text{-}Adm)_{18}(PPh_2py)_4](BPh_4)_2 + 2Cl^-$.

Characterization

The optical absorption spectra of nanoclusters were recorded using an Agilent 8453 diode array spectrometer.

Electrospray ionization mass spectrometry (ESI-MS) measurements were performed by using a Waters XEVO G2-XS QTof mass spectrometer. The sample was directly infused into the chamber at 5 μL min^{-1}. For preparing the ESI samples, nanoclusters were dissolved in CH_2Cl_2 (1 mg mL^{-1}) and diluted (v/v = 1 : 1) with CH_3OH.

Infrared (IR) measurements were recorded on a Bruker Vertex 80sv Fourier transform IR spectrometer.

X-ray crystallography

The data collection for single-crystal X-ray diffraction (SC-XRD) of **Ag_{29}-PPh_2py** was carried out on a Bruker Smart APEX II CCD diffractometer under a nitrogen flow, using graphite-monochromatized Mo Kα radiation (λ = 0.71073 Å). The data collection for single-crystal X-ray diffraction (SC-XRD) of **Pt_1Ag_{28}-PPh_2py** was carried out on a Stoe Stadivari diffractometer under a nitrogen flow, using graphite-monochromatized Cu Kα radiation (λ = 1.54186 Å). Data reductions and absorption corrections were performed using the SAINT and SADABS programs, respectively. The structure was solved by direct methods and refined with full-matrix least squares on F^2 using the SHELXTL software package. All non-hydrogen atoms were refined anisotropically, and all the hydrogen atoms were set in geometrically calculated positions and refined isotropically using a riding model. All crystal structures were treated with PLATON SQUEEZE. The diffuse electron densities from these residual solvent molecules were removed. The CCDC number of the **Ag_{29}-PPh_2py** nanocluster is 2115749. The CCDC number of the **Pt_1Ag_{28}-PPh_2py** nanocluster is 2117814.

3 Results and discussion

Ag_{29}-PPh_3 was prepared by a literature method.[46] Although the **Ag_{29}-PPh_3** nanocluster was uncrystallizable because of its weak stability, several of its alloyed derivatives have been structurally determined, including **Pt_1Ag_{28}-PPh_3**, Au_1Ag_{28}(S-Adm)$_{18}(PPh_3)_4$, and $Pt_1Ag_{12}Cu_{16}$(S-Adm)$_{18}(PPh_3)_4$.[44–46] In this context, alloying has been used as an efficient approach to improve the stability of the M_{29} framework.[46] Fig. 1 depicts the proposed structure of **Ag_{29}-PPh_3**. Of note, the Ag_{13} kernel in **Ag_{29}-PPh_3** might follow a FCC (face-centered cubic) configuration for two reasons: (i) the

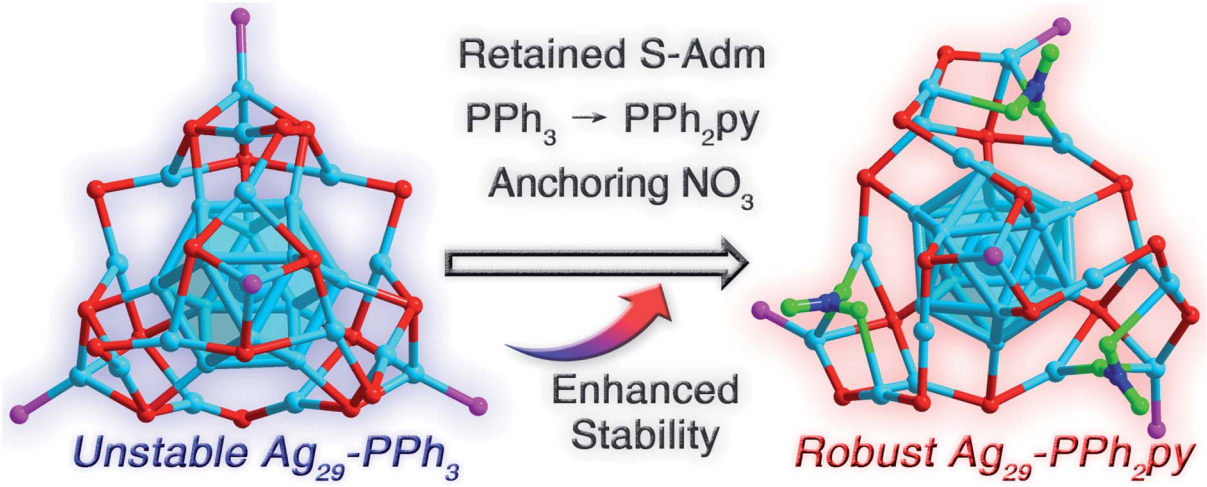

Fig. 1 Structural comparison between unstable **Ag_{29}-PPh_3** and robust **Ag_{29}-PPh_2py**. Compared with **Ag_{29}-PPh_3**, the **Ag_{29}-PPh_2py** nanocluster contained retained S-Adm ligands, while the surface PPh_3 ligands were altered to PPh_2py, and several NO_3 ligands were arranged on the nanocluster surface. Color legends: light blue sphere, Ag; red sphere, S; magenta sphere, P; blue sphere, N; green sphere, O. For clarity, all C and H atoms are omitted. Of note, the structure of **Ag_{29}-PPh_3** is proposed in this figure.

consistent FCC configuration of the M_{13} kernel in PPh_3 and S-Adm co-stabilized M_{29} nanoclusters,[44–46] and (ii) the different absorption profiles of **Ag_{29}-PPh_3** and **Ag_{29}-PPh_2py** (discussed below). However, such a verification calls for more experimental efforts.

At the same time, we unremittingly made efforts to stabilize the homo-silver Ag_{29} and determine its atomically precise structure. Considering that (i) the unchanging S-Adm ligand could retain the basic framework of the Ag_{29} nanocluster[47,48] and (ii) the introduction of N-coordination sites in original ligands would generate new N–metal interactions that might enhance the structural robustness,[49–52] we were motivated to substitute the PPh_3 ligand with PPh_2py while retaining the S-Adm ligand in the nanocluster synthesis. A new Ag_{29} nanocluster, formulated as $Ag_{29}(S\text{-}Adm)_{15}(NO_3)_3(PPh_2py)_4$ (**Ag_{29}-PPh_2py**), was synthesized and further structurally determined owing to its high stability (Fig. 1 and S1†).

Compared with **Ag_{29}-PPh_3**, **Ag_{29}-PPh_2py** contained three fewer S-Adm ligands and three more NO_3 ligands, and the number of the phosphine ligands retained was four (Fig. 1). Because of the interactions between N (in PPh_2py) and Ag (in the cluster), the surface structure of **Ag_{29}-PPh_2py** displayed more obvious distortion relative to **Ag_{29}-PPh_3** (Fig. 1 and S2†). Besides, three NO_3 ligands were observed on the nanocluster surface *via* Ag–O interactions. For the three O atoms in each NO_3, the two inward O linked to two Ag atoms or one Ag atom, while the outward O was naked (Fig. 1 and S2†). The presence of NO_3 in the cluster system has been verified by IR measurement (Fig. S3†). ESI-MS measurement was performed to validate the molecular composition and determine the valence state of the nanocluster. As shown in Fig. S4,† the experimental mass signals at 2292.30 and 2271.64 Da matched well with the theoretical results of $[Ag_{29}(S\text{-}Adm)_{15}(NO_3)_3(PPh_2py)_4]^{3+}$ and $[Ag_{29}(S\text{-}Adm)_{15}(NO_3)_2(PPh_2py)_4]^{3+}$, respectively. In this context, the NO_3 ligand on the nanocluster surface was more prone to be dissociated relative to S-Adm and PPh_2py ligands. Besides, the "+3" valence state of **Ag_{29}-PPh_2py** was tallied with the presence of $3SbF_6^-$ counterions with an Ag_{29} cluster molecule in the crystal lattice (Fig. S1†). According to the valence state of the **Ag_{29}-PPh_2py** nanocluster, its nominal electron count was determined to be 8,[53] *i.e.*, 29(Ag) − 15(SR) − 3(NO_3) − 3(charge) = 8*e*, the same as that of **Ag_{29}-PPh_3**.

Structurally, the **Ag_{29}-PPh_2py** nanocluster contains an icosahedral Ag_{13} kernel (Fig. 2A). Of note, for other structurally determined $M_{29}(S\text{-}Adm)_{18}(PR_3)_4$ nanoclusters, their Ag_{13} kernels follow a FCC configuration.[46] The difference between these two kernel configurations originates from their distinguishable surface environments *via* a "surface-kernel structure transfer effect". The Ag_{13} kernel of **Ag_{29}-PPh_2py** is first wrapped by three same $Ag_4(S\text{-}Adm)_2(PPh_2py)_1$ motif structures that are further fixed by three S-Adm bridges (Fig. 2B and C), giving rise to an $Ag_{25}(S\text{-}Adm)_9(PPh_2py)_3$ structure (Fig. 2D). Such three $Ag_4(S\text{-}Adm)_2(PPh_2py)_1$ motifs or three S-Adm bridges are in C_3 axial symmetry. Besides, an $Ag_4(S\text{-}Adm)_6(PPh_2py)_1$ surface unit caps the $Ag_{25}(S\text{-}Adm)_9(PPh_2py)_3$ structure to present an $Ag_{29}(S\text{-}Adm)_{15}(PPh_3py)_4$ structure (Fig. 2E and F). In this context, the four PPh_2py ligands follow different bonding modes in the nanocluster framework: three PPh_2py are dually bonded onto the nanocluster *via* both Ag–P and Ag–N interactions, while the remaining one is singly bonded onto the nanocluster vertex *via* the Ag–P interaction (Fig. S2†). Of note, the $Ag_{29}(S\text{-}Adm)_{15}(PPh_3py)_4$ structure is still bare to a certain extent, and three NO_3 ligands, which originated from the $AgNO_3$ reactant, are further anchored onto the nanocluster surface (Fig. 2G), making the Ag_{29} kernel fully protected and yielding the overall structure of **Ag_{29}-PPh_2py** (Fig. 2H). The complete structure of **Ag_{29}-PPh_2py** follows a C_3 axial symmetry, and the axis of the symmetry passes through the vertex P and the innermost Ag atoms (Fig. S5†).

In the crystal lattice of **Ag_{29}-PPh_2py**, two nanocluster enantiomers were observed, labeled as the *R*-nanocluster enantiomer

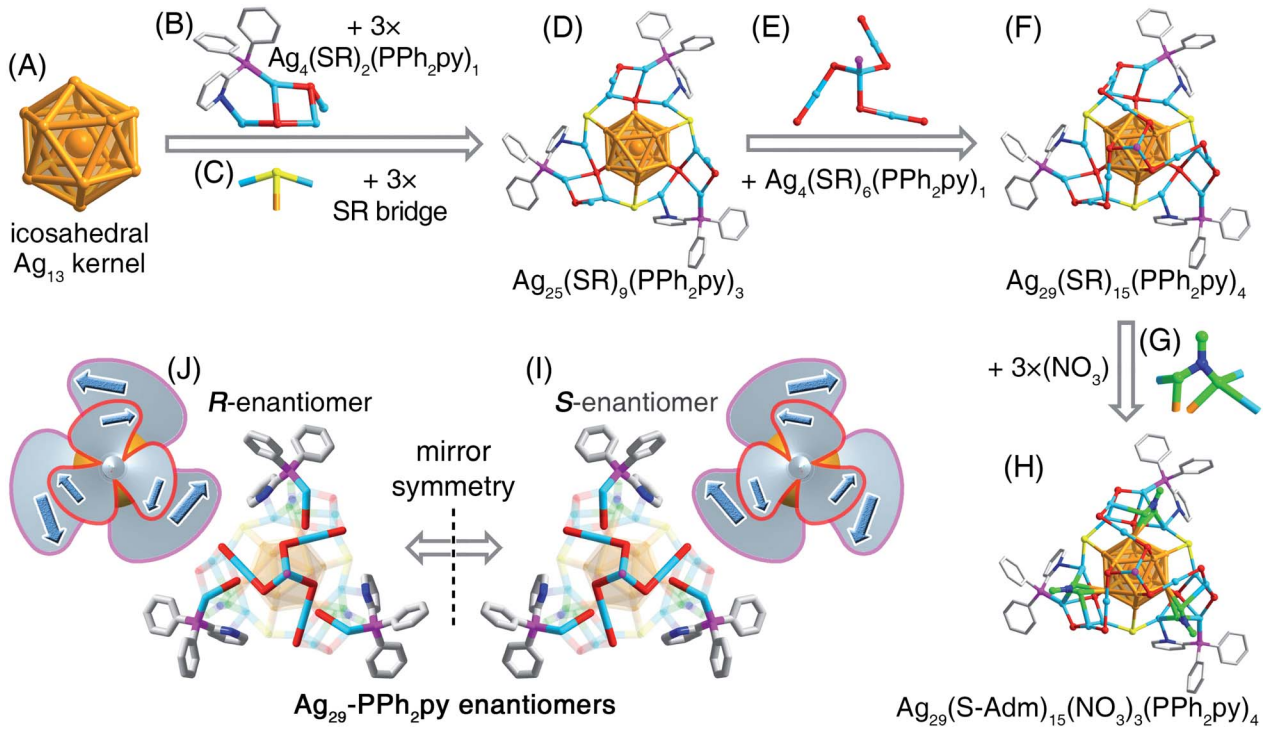

Fig. 2 Structural anatomy of the Ag_{29}-PPh_2py nanocluster. (A) The icosahedral Ag_{13} kernel. (B) and (C) The $Ag_4(S\text{-}Adm)_2(PPh_2py)_1$ surface and S-Adm bridge-like units. (D) The $Ag_{25}(S\text{-}Adm)_9(PPh_2py)_3$ structure. (E) The $Ag_4(S\text{-}Adm)_6(PPh_2py)_1$ surface unit. (F) $Ag_{29}(S\text{-}Adm)_{15}(PPh_3py)_4$ structure. (G) The surface NO_3 ligand. (H) Overall structure of the **Ag_{29}-PPh_2py** nanocluster. (J) and (I) The **Ag_{29}-PPh_2py** nanocluster enantiomers. Color legends: orange sphere, kernel Ag; light blue sphere, surface Ag; red/yellow sphere, S; magenta sphere, P; blue sphere, N; green sphere, O. For clarity, all H atoms and several C atoms are omitted.

and *S*-nanocluster enantiomer in Fig. 2I and J. Each type of enantiomer displayed a bilayer rotation: (i) for the *S*-nanocluster enantiomer, the inner-layer (*i.e.*, the $Ag_4(S\text{-}Adm)_6(PPh_2py)_1$) was counterclockwise while the outer-layer (*i.e.*, assembly of three surface $Ag_1(S\text{-}Adm)_1(PPh_2py)_1$) was clockwise (Fig. 2I); (ii) for the *R*-nanocluster enantiomer, the rotations of the inner-layer and outer-layer were opposite to those of the *S*-nanocluster enantiomer (Fig. 2J). Since the quantities of *R*- and *S*-nanocluster enantiomers are the same in the crystal lattice, the nanocluster samples were racemic.

The **Ag_{29}-PPh_3** and **Ag_{29}-PPh_2py** nanoclusters with distinguishable kernel structures and surface environments exhibited different optical absorptions. The CH_2Cl_2 solution of **Ag_{29}-PPh_3** showed an intense absorption at 413 nm and a shoulder band at 506 nm (Fig. S6,† black line). By comparison, the CH_2Cl_2 solution of **Ag_{29}-PPh_3** showed several apparent UV-vis signals at 401, 438, and 530 nm (Fig. S6,† red line). The difference in optical absorptions of these two Ag_{29} nanoclusters suggested their distinct electronic structures.[54,55] The photoluminescence properties of **Ag_{29}-PPh_3** and **Ag_{29}-PPh_2py** nanoclusters were further compared. As shown in Fig. S7,† the CH_2Cl_2 solution of **Ag_{29}-PPh_3** was red emissive with an intense signal at 622 nm. By comparison, the **Ag_{29}-PPh_2py** was non-emissive in the solution state. The different photophysical properties originated from their distinct electronic structures.[54,55]

The thermal stability of these two Ag_{29} nanoclusters was then compared in air. As shown in Fig. 3A, the characteristic optical peaks of **Ag_{29}-PPh_3** continuously decreased in the first three hours and completely disappeared within six hours, demonstrating the decomposition of the nanoclusters. In this context, the **Ag_{29}-PPh_3** nanocluster was unstable. In vivid contrast, the optical absorptions of **Ag_{29}-PPh_2py** remained unchanged for 24 hours (Fig. 3B), which suggested the high robustness of this nanocluster. Besides, the difference in stability was primarily responsible for the crystallographic discrepancy of these two Ag_{29} nanoclusters: the **Ag_{29}-PPh_3** nanocluster was uncrystallizable, whereas the crystal structure of **Ag_{29}-PPh_2py** was successfully determined.

Collectively, as depicted in Fig. 4A, two approaches have been presented to endow the unstable **Ag_{29}-PPh_3** nanocluster with enhanced stability: (i) the metal control approach (*e.g.*, from unstable **Ag_{29}-PPh_3** to stable **Pt_1Ag_{28}-PPh_3**),[46] and (ii) the ligand control approach (*i.e.*, from unstable **Ag_{29}-PPh_3** to stable **Ag_{29}-PPh_2py**). These two disparately stabilizing approaches raised an interesting question: which type of the Pt_1Ag_{28} nanocluster would be generated when the metal control and the ligand control were performed simultaneously in the synthesis (Fig. 4B)?

As inspired by the aforementioned results, two types of Pt_1Ag_{28} nanoclusters with different surface environments might be generated (Fig. 4B): $Pt_1Ag_{28}(S\text{-}Adm)_{18}(PPh_2py)_4$ with a maintained framework or $Pt_1Ag_{28}(S\text{-}Adm)_{15}(NO_3)_3(PPh_2py)_4$ with a twisted framework. After the crystallographic analysis, we determined its structure as the framework-retained Pt_1Ag_{28}(S-

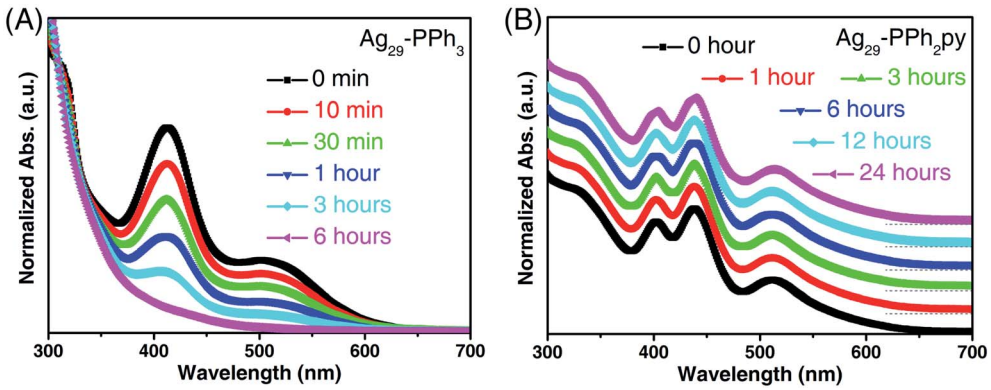

Fig. 3 Stability of different Ag_{29} nanoclusters. (A) Time-dependent optical absorptions of **Ag_{29}-PPh_3** in CH_2Cl_2 in air. (B) Time-dependent optical absorptions of **Ag_{29}-PPh_2py** in CH_2Cl_2 in air.

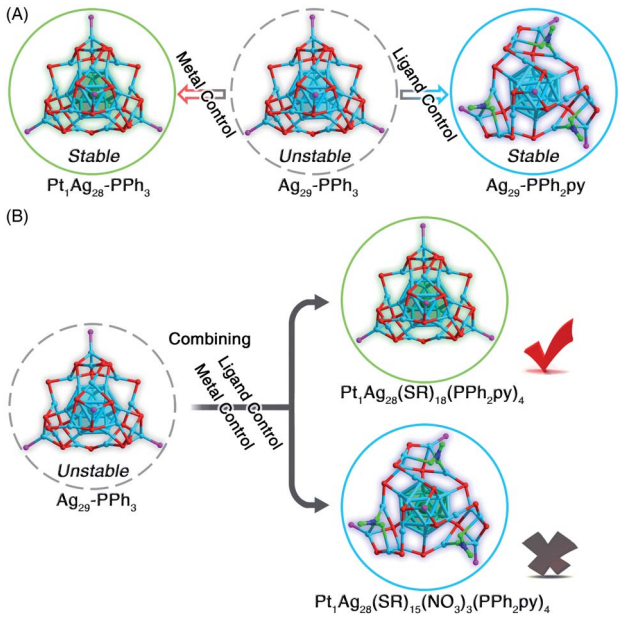

Fig. 4 Metal control *versus* ligand control on the Ag_{29} nanocluster template. (A) From unstable **Ag_{29}-PPh_3** to stable **Pt_1Ag_{28}-PPh_3** *via* metal control, or from unstable **Ag_{29}-PPh_3** to stable **Ag_{29}-PPh_2py** *via* ligand control. (B) From unstable **Ag_{29}-PPh_3** to stable **Pt_1Ag_{28}-PPh_2py** *via* both metal control and ligand control. Color legends: light blue sphere, Ag; dark green sphere, Pt; red sphere, S; magenta sphere, P; blue sphere, N; green sphere, O. For clarity, all C and H atoms are omitted.

$Adm)_{18}(PPh_2py)_4$ (**Pt_1Ag_{28}-PPh_2py** for short). The structure of **Pt_1Ag_{28}-PPh_2py** was almost the same as that of **Pt_1Ag_{28}-PPh_3** (Fig. S8†).[44,46] Although the four PPh_2py ligands in **Pt_1Ag_{28}-PPh_2py** exposed N coordination sites, these N sites remained uncoordinated in the nanocluster formation (Fig. S8†). Consequently, in the competition between metal control and ligand control in this nanocluster system, the metal control seized a dominant position (Fig. 4B). In other words, when the Pt heteroatom was introduced into the innermost region of the nanocluster, the M_{29} structure was robust enough to hinder the formation of surface Ag–N interactions, which resulted in a retained cluster framework without any distortion. Besides, in the previously reported intercluster transformation from **Pt_1Ag_{28}-PPh_3** into $Pt_1Ag_{28}(BDT)_{12}(PPh_3)_4$ (BDT = 1,3-benzenedithiolate), the presence of BDT afforded the kernel transformation from FCC into icosahedron.[56] In this context, for the Pt_1Ag_{28} cluster template, the bidentate thiolate ligand (*i.e.*, BDT) showed enhanced ability for directing the nanocluster configuration relative to the bidentate phosphine ligand (*i.e.*, PPh_2py).

The **Ag_{29}-PPh_2py** nanocluster molecules followed a crystallographic pattern of "lamellar eutectic" between *R*-nanocluster and *S*-nanocluster enantiomers, viewed from both *x* and *y* axes (Fig. S9A–C†). The interlayer distance along the *z* axis was determined to be 34.064 Å (from cluster kernel to cluster kernel, as shown in Fig. S9B†). Significantly, the supracrystal lattice of **Ag_{29}-PPh_2py** showed several intercluster channels with the same diameter of 18.875 Å from the (001) crystalline plane (Fig. 5A and S9D†), which was reminiscent of the behavior of MOFs (metal–organic frameworks).[57,58] However, the channel diameter should be remarkably less than 18.875 Å due to the presence of carbon tails from peripheral ligands of nanoclusters (Fig. S10†). The intercluster channel was constructed by symmetrically assembling six cluster molecules into a hexagon, where three molecules were *R*-nanocluster enantiomers (marked in orange in Fig. 5B), while the other three were *S*-nanocluster enantiomers (marked in blue in Fig. 5B). Specifically, the intercluster hexagon was composed of two cluster-based triangles in parallel planes in opposite directions, and each triangle contained three cluster molecules in the same enantiomeric configuration (Fig. 5B and C). The intermolecular distance of the cluster-based triangle was 22.224 Å, and the interlayer distance between two adjacent triangles was 18.816 Å (Fig. 5B and C). Furthermore, the arrangement of SbF_6^- counterions in the supracrystal lattice was analyzed. As shown in Fig. S11,† 2/3 of SbF_6^- counterions were uniformly organized in the intercluster channels while the others were packed along the C_3 axis of symmetry of **Ag_{29}-PPh_2py** nanoclusters. Of note, such a hexagon-like crystallographic packing of **Ag_{29}-PPh_2py** cluster molecules in the supracrystal lattice was unique, which has yet been detected in other M_{29} nanocluster crystals.[44–46,48,59,60] For example, for the crystal lattice of **Pt_1Ag_{28}-PPh_2py**, the nanocluster molecules were packed in

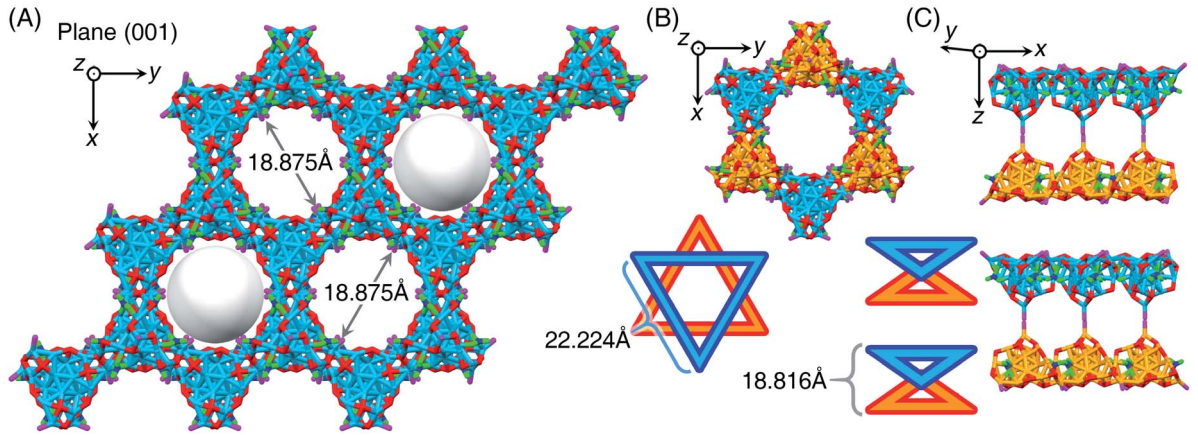

Fig. 5 Packing of Ag_{29}-PPh_2py in the supracrystal lattice. (A) Crystalline packing of **Ag_{29}-PPh_2py**, viewed from the (001) plane. (B) Vertical and (C) lateral views of the aggregation pattern of **Ag_{29}-PPh_2py** molecules in the supracrystal lattice. Color legends: light blue sphere, Ag in the *S*-nanocluster enantiomer; orange sphere, Ag in the *R*-nanocluster enantiomer; red sphere, S; magenta sphere, P; blue sphere, N; green sphere, O. For clarity, all C and H atoms are omitted.

a layered assembly mode from the *x* axis, *y* axis, or *z* axis, and no intercluster channel was detected (Fig. S12†). In this context, such unique intercluster channels may render the **Pt_1Ag_{28}-PPh_2py** crystals potential nanomaterials for gas adsorption-related applications.[61–65]

4 Conclusions

In summary, a strategy termed "surface environment complication" has been exploited to render unstable Ag_{29} highly robust. The surface structure of unstable $Ag_{29}(S\text{-}Adm)_{18}(PPh_3)_4$ underwent directional distortion due to the generation of Ag–N interactions by substituting the monodentate PPh_3 ligand with bidentate PPh_2py. Besides, three NO_3 ligands were anchored onto the nanocluster surface to entirely protect the Ag_{29} kernel, yielding a new $Ag_{29}(S\text{-}Adm)_{15}(NO_3)_3(PPh_2py)_4$ nanocluster with high robustness. Owing to its enhanced stability, the $Ag_{29}(S\text{-}Adm)_{15}(NO_3)_3(PPh_2py)_4$ nanocluster was crystallizable, and its atomically precise structure was successfully determined. On the supramolecular level, the $Ag_{29}(S\text{-}Adm)_{15}(NO_3)_3(PPh_2py)_4$ nanocluster molecules followed a unique crystallographic packing mode and displayed several intercluster channels. This study thus presented a novel strategy for tailoring the surface environment of metal nanoclusters, and also provided fundamental insights into the controllable synthesis of highly robust silver nanoclusters. Future work will focus on promoting this strategy to other ligand-protected metal nanoclusters.

Data availability

All the data supporting this article have been included in the main text and the ESI.†

Author contributions

C. X. and Q. Y. carried out the experiments and analyzed the data. X. W., H. L. and H. S. assisted in the analysis. X. K. and M. Z. designed the project, analyzed the data, and wrote the manuscript.

Conflicts of interest

There are no conflicts to declare.

Acknowledgements

We acknowledge the financial support of the NSFC (21631001, 21871001, and 22101001), the Ministry of Education, and the University Synergy Innovation Program of Anhui Province (GXXT-2020-053).

Notes and references

1 R. Jin, C. Zeng, M. Zhou and Y. Chen, *Chem. Rev.*, 2016, **116**, 10346–10413.
2 I. Chakraborty and T. Pradeep, *Chem. Rev.*, 2017, **117**, 8208–8271.
3 X. Kang, Y. Li, M. Zhu and R. Jin, *Chem. Soc. Rev.*, 2020, **49**, 6443–6514.
4 Q. Yao, T. Chen, X. Yuan and J. Xie, *Acc. Chem. Res.*, 2018, **51**, 1338–1348.
5 A. W. Cook and T. W. Hayton, *Acc. Chem. Res.*, 2018, **51**, 2456–2464.
6 N. Xia and Z. Wu, *Chem. Sci.*, 2021, **12**, 2368–2380.
7 S. Takano and T. Tsukuda, *J. Am. Chem. Soc.*, 2021, **143**, 1683–1698.
8 S. Kenzler and A. Schnepf, *Chem. Sci.*, 2021, **12**, 3116–3129.
9 K. Kwak and D. Lee, *Acc. Chem. Res.*, 2019, **52**, 12–22.
10 B. Nieto-Ortega and T. Bürgi, *Acc. Chem. Res.*, 2018, **51**, 2811–2819.
11 M. Agrachev, M. Ruzzi, A. Venzo and F. Maran, *Acc. Chem. Res.*, 2019, **52**, 44–52.
12 T. Higaki, Q. Li, M. Zhou, S. Zhao, Y. Li, S. Li and R. Jin, *Acc. Chem. Res.*, 2018, **51**, 2764–2773.

13 X. Kang and M. Zhu, *Chem. Soc. Rev.*, 2019, **48**, 2422–2457.
14 N. A. Sakthivel and A. Dass, *Acc. Chem. Res.*, 2018, **51**, 1774–1783.
15 Y. Liu, X. Chai, X. Cai, M. Chen, R. Jin, W. Ding and Y. Zhu, *Angew. Chem., Int. Ed.*, 2018, **57**, 9775–9779.
16 S. Ito, S. Takano and T. Tsukuda, *J. Phys. Chem. Lett.*, 2019, **10**, 6892–6896.
17 Y. Wang, E. Makkonen, X. Chen and T. Bürgi, *Chem. Sci.*, 2021, **12**, 9413–9419.
18 W. Fei, S. Antonello, T. Dainese, A. Dolmella, M. Lahtinen, K. Rissanen, A. Venzo and F. Maran, *J. Am. Chem. Soc.*, 2019, **141**, 16033–16045.
19 M. Hesari, H. Ma and Z. Ding, *Chem. Sci.*, 2021, **12**, 14540–14545.
20 H. Yoshida, M. Ehara, U. D. Priyakumar, T. Kawai and T. Nakashima, *Chem. Sci.*, 2020, **11**, 2394–2400.
21 W. Kurashige, Y. Niihori, S. Sharma and Y. Negishi, *Coord. Chem. Rev.*, 2016, **320**, 238–250.
22 J. Yan, B. K. Teo and N. Zheng, *Acc. Chem. Res.*, 2018, **51**, 3084–3093.
23 M. H. Naveen, R. Khan and J. H. Bang, *Chem. Mater.*, 2021, **33**, 7595–7612.
24 T. Kawawaki, Y. Kataoka, S. Ozaki, M. Kawachi, M. Hirata and Y. Negishi, *Chem. Commun.*, 2021, **57**, 417–440.
25 B. Bhattarai, Y. Zaker, A. Atnagulov, B. Yoon, U. Landman and T. P. Bigioni, *Acc. Chem. Res.*, 2018, **51**, 3104–3113.
26 L. He and T. Dong, *CrystEngComm*, 2021, **23**, 7369–7379.
27 C. P. Joshi, M. S. Bootharaju, M. J. Alhilaly and O. M. Bakr, *J. Am. Chem. Soc.*, 2015, **137**, 11578–11581.
28 A. Desireddy, B. E. Conn, J. Guo, B. Yoon, R. N. Barnett, B. M. Monahan, K. Kirschbaum, W. P. Griffith, R. L. Whetten, U. Landman and T. P. Bigioni, *Nature*, 2013, **501**, 399–402.
29 H. Yang, Y. Wang, H. Huang, L. Gell, L. Lehtovaara, S. Malola, H. Häkkinen and N. Zheng, *Nat. Commun.*, 2013, **4**, 2422.
30 L. G. AbdulHalim, M. S. Bootharaju, Q. Tang, S. Del Gobbo, R. G. AbdulHalim, M. Eddaoudi, D.-e. Jiang and O. M. Bakr, *J. Am. Chem. Soc.*, 2015, **137**, 11970–11975.
31 K.-G. Liu, X.-M. Gao, T. Liu, M.-L. Hu and D.-e. Jiang, *J. Am. Chem. Soc.*, 2020, **142**, 16905–16909.
32 M. Qu, H. Li, L.-H. Xie, S.-T. Yan, J.-R. Li, J.-H. Wang, C.-Y. Wei, Y.-W. Wu and X.-M. Zhang, *J. Am. Chem. Soc.*, 2017, **139**, 12346–12349.
33 F. Tian and R. Chen, *J. Am. Chem. Soc.*, 2019, **141**, 7107–7114.
34 A. Jana, M. Jash, A. K. Poonia, G. Paramasivam, M. R. Islam, P. Chakraborty, S. Antharjanam, J. Machacek, S. Ghosh, K. N. V. D. Adarsh, T. Base and T. Pradeep, *ACS Nano*, 2021, **15**, 15781–15793.
35 X. Liu, J. Chen, J. Yuan, Y. Li, J. Li, S. Zhou, C. Yao, L. Liao, S. Zhuang, Y. Zhao, H. Deng, J. Yang and Z. Wu, *Angew. Chem., Int. Ed.*, 2018, **57**, 11273–11277.
36 L. Qin, F. Sun, X. Ma, G. Ma, Y. Tang, L. Wang, Q. Tang, R. Jin and Z. Tang, *Angew. Chem., Int. Ed.*, 2021, **60**, 26136–26141.
37 X.-Q. Liang, Y.-Z. Li, Z. Wang, S.-S. Zhang, Y.-C. Liu, Z.-Z. Cao, L. Feng, Z.-Y. Gao, Q.-W. Xue, C.-H. Tung and D. Sun, *Nat. Commun.*, 2021, **12**, 4966.
38 S.-F. Yuan, C.-Q. Xu, W.-D. Liu, J.-X. Zhang, J. Li and Q.-M. Wang, *J. Am. Chem. Soc.*, 2021, **143**, 12261–12267.
39 R. S. Dhayal, J.-H. Liao, Y.-C. Liu, M. H. Chiang, S. Kahlal, J.-Y. Saillard and C. W. Liu, *Angew. Chem., Int. Ed.*, 2015, **54**, 3702–3706.
40 H. Yang, Y. Wang, X. Chen, X. Zhao, L. Gu, H. Huang, J. Yan, C. Xu, G. Li, J. Wu, A. J. Edwards, B. Dittrich, Z. Tang, D. Wang, L. Lehtovaara, H. Häkkinen and N. Zheng, *Nat. Commun.*, 2016, **7**, 12809.
41 Y. Tao, M. Li, J. Ren and X. Qu, *Chem. Soc. Rev.*, 2015, **44**, 8636–8663.
42 Y. Nie, X. Tao, Y. Zhou, X. Yuan, Y. Zhuo, Y.-q. Chai and R. Yuan, *Anal. Chem.*, 2021, **93**, 1120–1125.
43 P. Lopez, H. H. Lara, S. M. Mullins, D. M. Black, H. M. Ramsower, M. M. Alvarez, T. L. Williams, X. Lopez-Lozano, H.-C. Weissker, A. P. García, I. L. Garzón, B. Demeler, J. L. Lopez-Ribot, M. J. Yacamán and R. L. Whetten, *ACS Appl. Nano Mater.*, 2018, **1**, 1595–1602.
44 X. Kang, M. Zhou, S. Wang, S. Jin, G. Sun, M. Zhu and R. Jin, *Chem. Sci.*, 2017, **8**, 2581–2587.
45 X. Kang, L. Huang, W. Liu, L. Xiong, Y. Pei, Z. Sun, S. Wang, S. Wei and M. Zhu, *Chem. Sci.*, 2019, **10**, 8685–8693.
46 X. Kang, X. Wei, S. Jin, Q. Yuan, X. Luan, Y. Pei, S. Wang, M. Zhu and R. Jin, *Proc. Natl. Acad. Sci. U. S. A.*, 2019, **116**, 18834–18840.
47 X. Kang, S. Jin, L. Xiong, X. Wei, M. Zhou, C. Qin, Y. Pei, S. Wang and M. Zhu, *Chem. Sci.*, 2020, **11**, 1691–1697.
48 X. Kang, X. Wei, S. Wang and M. Zhu, *Inorg. Chem.*, 2020, **59**, 8736–8743.
49 Y. Jin, C. Zhang, X.-Y. Dong, S.-Q. Zang and T. C. W. Mak, *Chem. Soc. Rev.*, 2021, **50**, 2297–2319.
50 R.-W. Huang, Y.-S. Wei, X.-Y. Dong, X.-H. Wu, C.-X. Du, S.-Q. Zang and T. C. W. Mak, *Nat. Chem.*, 2017, **9**, 689–697.
51 Z. Lei, X.-L. Pei, Z.-G. Jiang and Q.-M. Wang, *Angew. Chem., Int. Ed.*, 2014, **53**, 12771–12775.
52 M. J. Alhilaly, R.-W. Huang, R. Naphade, B. Alamer, M. N. Hedhili, A.-H. Emwas, P. Maity, J. Yin, A. Shkurenko, O. F. Mohammed, M. Eddaoudi and O. M. Bakr, *J. Am. Chem. Soc.*, 2019, **141**, 9585–9592.
53 M. Walter, J. Akola, O. Lopez-Acevedo, P. D. Jadzinsky, G. Calero, C. J. Ackerson, R. L. Whetten, H. Grönbeck and H. Häkkinen, *Proc. Natl. Acad. Sci. U. S. A.*, 2008, **105**, 9157–9162.
54 Q. Tang, G. Hu, V. Fung and D.-e. Jiang, *Acc. Chem. Res.*, 2018, **51**, 2793–2802.
55 C. M. Aikens, *Acc. Chem. Res.*, 2018, **51**, 3065–3073.
56 M. S. Bootharaju, S. M. Kozlov, Z. Cao, A. Shkurenko, A. M. El-Zohry, O. F. Mohammed, M. Eddaoudi, O. M. Bakr, L. Cavallo and J.-M. Basset, *Chem. Mater.*, 2018, **30**, 2719–2725.
57 O. M. Yaghi, M. O'Keeffe, N. W. Ockwig, H. K. Chae, M. Eddaoudi and J. Kim, *Nature*, 2003, **423**, 705–714.
58 Q. Yang, Q. Xu and H.-L. Jiang, *Chem. Soc. Rev.*, 2017, **46**, 4774–4808.
59 X. Kang, X. Wei, S. Jin, S. Wang and M. Zhu, *Inorg. Chem.*, 2021, **60**, 4198–4206.

60 X. Kang, F. Xu, X. Wei, S. Wang and M. Zhu, *Sci. Adv.*, 2019, **5**, eaax7863.
61 R. Custelcean, *Chem. Sci.*, 2021, **12**, 12518–12528.
62 B. Hua, Y. Ding, L. O. Alimi, B. Moosa, G. Zhang, W. S. Baslyman, J. Sessler and N. M. Khashab, *Chem. Sci.*, 2021, **12**, 12286–12291.
63 X. Wei, X. Kang, Q. Yuan, C. Qin, S. Jin, S. Wang and M. Zhu, *Chem. Mater.*, 2019, **31**, 4945–4952.
64 X. Wei, X. Kang, Z. Zuo, F. Song, S. Wang and M. Zhu, *Nat. Sci. Rev.*, 2021, **8**, nwaa077.
65 G. Liu, W. S. Y. Wong, M. Kraft, J. W. Ager, D. Vollmer and R. Xu, *Chem. Soc. Rev.*, 2021, **50**, 10674–10699.